

# Mechanisms Affecting the Transition from Shallow to Deep Convection over Land: Inferences from Observations of the Diurnal Cycle Collected at the ARM Southern Great Plains Site

YUNYAN ZHANG AND STEPHEN A. KLEIN

*Lawrence Livermore National Laboratory, Livermore, California*

(Manuscript received 30 October 2009, in final form 14 May 2010)

## ABSTRACT

Summertime observations for 11 yr from the Atmospheric Radiation Measurement (ARM) Climate Research Facility Southern Great Plains (SGP) site are used to investigate mechanisms controlling the transition from shallow to deep convection over land. It is found that a more humid environment immediately above the boundary layer is present before the start of late afternoon heavy precipitation events. The higher moisture content is brought by wind from the south. Greater boundary layer inhomogeneity in moist static energy, temperature, moisture, and horizontal wind before precipitation begins is correlated to larger rain rates at the initial stage of precipitation. In an examination of afternoon rain statistics, higher relative humidity above the boundary layer is correlated to an earlier onset and longer duration of afternoon precipitation events, whereas greater boundary layer inhomogeneity and atmospheric instability in the 2–4-km layer above the surface are positively correlated to the total rain amount and the maximum rain rate. Although other interpretations may be possible, these observations are consistent with theories for the transition from shallow to deep convection that emphasize the role of a moist lower free troposphere and boundary layer inhomogeneity.

## 1. Introduction

Convection and clouds are key processes that regulate the global energy and water budgets. The diurnal timing of convection is very important, because the associated clouds strongly interact with both solar and infrared radiation. Numerous observations show that over land the diurnal maxima of deep convection and precipitation occur frequently in the late afternoon or early evening (Dai et al. 1999; Soden 2000; Dai 2001; Yang and Slingo 2001; Nesbitt and Zipser 2003). It is generally accepted that the diurnal variation over land is closely related to the solar heating of surface and atmospheric boundary layer and thus is stronger in summertime.

Convection and clouds cannot be explicitly simulated but are highly parameterized in conventional global climate models. The simulation of the diurnal cycle is an important measure of a climate model's performance (Randall et al. 1991; Yang and Slingo 2001; Tian et al.

2004; Dai 2006; Zhang et al. 2008). Traditional moist convection parameterizations are often associated with atmospheric instability in terms of convective available potential energy (CAPE) (Arakawa and Schubert 1974; Zhang and McFarlane 1995) or large-scale moisture convergence (Kuo 1965, 1974; Tiedtke 1989). A well-known problem is that climate models usually cannot produce the observed afternoon convective rainfall peak over land (Dai et al. 1999; Yang and Slingo 2001); instead, they usually simulate a quick onset of convective rainfall, before or at noon and in phase with the diurnal cycle of CAPE (Bechtold et al. 2004). Previous studies suggest that this deficiency is due to the lack of an intermediate stage involving shallow and middle-level topped cumulus and their associated effects, such as the gradual moistening of the free troposphere (Guichard et al. 2004). This reminds us that, to solve this timing problem, we need to know what atmospheric conditions favor different convection regimes, such as shallow versus deep convection. In other words, what makes shallow cumulus stay shallow, and what promotes the transition of shallow to deep convection?

Recently studies of cloud resolving model (CRM) or large-eddy simulation (LES), in which finescale cloud

---

*Corresponding author address:* Yunyan Zhang, PCMDI, Atmospheric, Earth, and Energy Division, Lawrence Livermore National Laboratory, Mail Code L-103, P.O. Box 808, Livermore, CA 94551.  
E-mail: zhang25@llnl.gov

processes can be explicitly resolved, have revealed several mechanisms on the transition from shallow to deep convection focusing on the influence of the following:

- free-tropospheric humidity, which influences the buoyancy of entraining cumulus clouds (Derbyshire et al. 2004; Kuang and Bretherton 2006);
- subdomain variability such as boundary layer cold pools driven by precipitation evaporation, which may promote further convection at gust front edges (Tompkins 2001; Chaboureau et al. 2004; Khairoutdinov and Randall 2006); and
- atmospheric instability at the cloud level when the transition from shallow to deep convection occurs (Houston and Niyogi 2007; Wu et al. 2009).

Considerable observational evidence also suggests that high values of lower-tropospheric humidity precede deep convection, especially over tropical oceans (Sherwood and Wahrlich 1999; Bretherton et al. 2004b; Mapes et al. 2006; Holloway and Neelin 2009). An association between the boundary layer inhomogeneity and deep convection has also been established from observations of stronger convection associated with squall lines (Wakimoto 1982), land–sea breezes (Kingsmill 1995), and mesoscale convective systems (Engerer and Stensrud 2008).

In this study, we use convective-regime-oriented composites from long-term observations over land to make a systematic assessment of these transition mechanisms. The Atmospheric Radiation Measurement (ARM; Stokes and Schwartz 1994; Ackerman and Stokes 2003) Climate Research Facility provides the necessary long-term comprehensive measurements at its Southern Great Plains (SGP) site. However, the coexistence of multiple convection regimes at various temporal and spatial scales complicates the analysis of SGP observations (Dong et al. 2005; Berg and Kassianov 2008). To assess theories for the transition, we are more interested in convection and clouds that are locally generated, limited in time to one diurnal cycle, and not significantly influenced by large-scale forcing. Thus, the two regimes of interest to us are fair-weather nonprecipitating shallow cumulus and late afternoon or early evening precipitating deep convection, which, as will be shown below, grows from shallow convection. Our working hypothesis is that, once an ensemble of observations is established for each of these regimes, the mechanisms affecting transition from shallow to deep convection would be revealed by comparing the statistics of environmental parameters between and within convection regimes. If successful, a more typical composite case of each regime might be set up for future CRM, LES, or single-column model (SCM) studies and provide information more relevant to the parameterization of

convection in climate models. In this paper, we try to answer two questions:

- 1) What environmental parameters differ between the two regimes, fair-weather shallow cumulus versus late afternoon deep convection, especially in the late morning a few hours before deep convection begins?
- 2) Is there any correlation between environmental parameters and rain statistics on days with late afternoon deep convection?

We expect that answers to these questions will provide useful inferences on the factors that favor the transition from shallow to deep convection. We also note that, although our study is suitable for midlatitude convection over land, our results might not apply to convection over other continental regions, such as the Amazon region with its dense vegetation coverage and stronger surface fluxes or coastal zones subject to the influence of land–sea breezes.

The remaining parts of the paper are as follows: the observations and convection-regime classification are presented in section 2. The comparison between the two regimes is shown in section 3; the influence of environmental parameters on the rain statistics of late afternoon deep convection is shown in section 4; discussions of transition mechanisms are presented in section 5; and conclusions including implications for convection parameterizations are discussed in section 6.

## 2. Data and methodology

### a. ARM observations

The original data from the ARM archive (available online at <http://www.arm.gov/data>) are processed to hourly averages. Unless otherwise stated, measurements are taken at SGP central facility (CF) or in the region within a 50-km radius of the CF as shown in Fig. 1. Specific data information is as follows:

- Precipitation from the Arkansas-Red Basin River Forecast Center (ABRFC; available online at <http://www.arm.gov/data/vaps/abrfc>) is based on radar-observed precipitation estimates combined with rain gauge reports (Fulton et al. 1998; Breidenbach et al. 1998). We use the hourly mean spatial average over the region within a 50-km radius of the CF.
- The vertical profile of cloud fraction is from Climate Modeling Best Estimate (CMBE; Xie et al. 2010; available online at [http://science.arm.gov/working\\_group/cpm/scm/best\\_estimate.html](http://science.arm.gov/working_group/cpm/scm/best_estimate.html)) Active Remote Sensing of Clouds data (ARSCL; Clothiaux et al. 2000, 2001; available online at <http://science.arm.gov/vaps/arscl.stm>). The data are based on retrievals applied

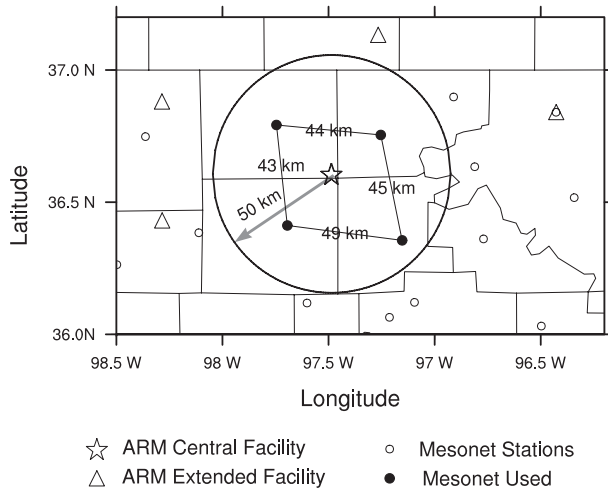


FIG. 1. The map of ARM facilities and Mesonet stations. Numbers denote the distance (km) between Mesonet stations. The circle encloses the area within 50 km of the ARM SGP CF and over which precipitation data are averaged.

to measurements made by the vertical pointing millimeter wavelength cloud radar, micropulse lidar, and laser ceilometers at the CF.

- Sounding data at the CF are from balloon sonde profiles whose water vapor is scaled with column-integrated precipitable water vapor (PWV) retrieved from the microwave radiometer (Turner et al. 1998; available online at <http://science.arm.gov/vaps/lssonde.stm>). Because the vertical resolution varies with meteorological conditions, data are regridded into a uniform resolution of 20 m to facilitate composite analysis.
- Column-integrated PWV and liquid water path (LWP) are from CMBE Microwave Radiometer Retrievals (MWRRET; Turner et al. 2007; available online at <http://science.arm.gov/vaps/mwrret.stm>).
- Surface sensible and latent heat fluxes are from the Bulk Aerodynamic Energy Balance Bowen Ratio data product (BAEBBR; Wesely et al. 1995; available online at <http://science.arm.gov/vaps/baebbr.stm>) retrieved from measurements of an EBBR station at the CF.
- Surface temperature, moisture, and winds are from the Surface Meteorological Observation Station (SMOS; available online at <http://www.arm.gov/instruments/smos>) at the CF and four surrounding Oklahoma Mesonet (OKM; Brock et al. 1995; available online at <http://www.arm.gov/instruments/okm>) stations shown in Fig. 1.
- Large-scale wind fields are from the National Centers for Environmental Prediction (NCEP) Model Output Location Time Series (MOLTS; available online at <http://www.arm.gov/instruments/molts>) data. They are provided by the Early Eta Model and its associated Eta Data Assimilation System.

We use the latest versions of value-added products to minimize the influence of measurement uncertainties. Forming a multiday composite also significantly reduces the impact of random errors contained in an individual observation.

### b. Warm-season convection-regime classification

Figure 2 shows the average diurnal cycle for 1176 days with valid observations of cloud fraction and surface precipitation rate from May to August in the years 1997–2007. The precipitation rate has a primary peak between 0200 and 0300 local standard time (LST) and a secondary peak between 1800 and 1900 LST. A similar diurnal behavior is found for the number of days with hourly precipitation rate in excess of  $1 \text{ mm day}^{-1}$ . High clouds tend to occur between late afternoon and the following noon with a maximum of about 22% at 11 km in late evening. Low clouds, usually about 10%–12% under 3 km, prefer to occur during daytime with a cloud base and top that rises gradually.

This diurnal variation hints at contributions from different convection regimes. The primary precipitation rate maximum between midnight and dawn is associated with eastward-propagating convection systems (Carbone et al. 2002; Jiang et al. 2006) initiated at the front range of the Rocky Mountains on the preceding afternoon. On the other hand, the secondary precipitation rate maximum during late afternoon or early evening might be a response to local surface heating (Jiang et al. 2006). With these thoughts in mind, we classify diurnal cycles for four convection regimes as follows:

- 1) Clear-sky day: The precipitation rate =  $0 \text{ mm day}^{-1}$  at all hours of the day and cloud fraction  $\leq 5\%$  at all levels between 0800 and 1600 LST. A single day is defined as the time between two successive local midnights.
- 2) Fair-weather nonprecipitating shallow cumulus day: The precipitation rate =  $0 \text{ mm day}^{-1}$  at all hours of the day, and shallow cumulus clouds are identified by Berg and Kassianov (2008), who first selected cumulus clouds based on fine temporal resolution ARSCL data at ARM SGP and then manually scrutinized cloud images taken by the Total Sky Imager (available online at <http://www.arm.gov/instruments/tsi>) to eliminate low cloud types other than shallow cumulus.
- 3) Late afternoon or early evening deep convection day: The diurnal maximum hourly precipitation rate  $\geq 1 \text{ mm day}^{-1}$  occurs between 1500 and 2000 LST and is at least twice more than the precipitation rate at any other hour of the day outside of 1500–2000 LST.

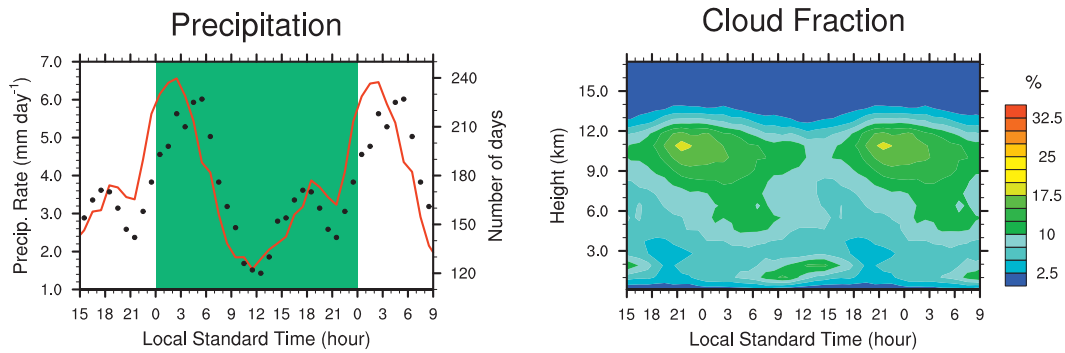


FIG. 2. Averaged warm-season diurnal cycle of (left) ABRFC surface precipitation and (right) CMBE ARSCL cloud fraction, for May–August of years 1997–2007. The red line in (left) denotes the hourly precipitation rate ( $\text{mm day}^{-1}$ ). (left) Black dots denote the number of days in which the hourly precipitation rate is  $>1 \text{ mm day}^{-1}$  during a certain hour; green shaded area identifies the diurnal cycle of interest; the 9-h periods before and after are also shown for the purpose of process continuity.

- 4) Nighttime deep convection day: The diurnal maximum hourly precipitation rate  $\geq 1 \text{ mm day}^{-1}$  and occurs between 0000 and 0700 LST.

There are 90, 95, 79, and 229 days for regimes 1–4, respectively, with no overlap. The number of days in the four regimes does not sum to the total days with valid observations, because there are other situations such as days with no precipitation but with clouds other than fair-weather shallow cumulus, days with drizzle, and days with heavy precipitation at hours that do not satisfy our criteria for late afternoon or nighttime deep convection. For the ensemble of late afternoon deep convection days, our selection criteria select many short-duration rain events generated within 50 km of the CF, as we desire; however, they do not exclude the possibility of organized convection or large-scale forcing beyond the 50-km scope, which we do not want to include. We examined animations of satellite infrared brightness temperature images provided by P. Minnis’s group at the National Aeronautics and Space Administration (NASA) Langley Center (available online at <http://www-angler.larc.nasa.gov/>) for days with late afternoon deep convection. A subjective judgment suggests that 15 days likely have features of convection organization or significant influence from large-scale forcing. Sensitivity tests show that the following results are not greatly affected if these days were omitted. As a result, we do not omit these days from the analysis in order to boost the sample size and statistical significance of the results.

Figure 3 shows the diurnal composites of precipitation and cloud fraction for regimes 1–4. On late afternoon deep convection days, precipitation starts from earlier afternoon, peaks at about  $21 \text{ mm day}^{-1}$  at 1630 LST, and diminishes after 2100 LST. On nighttime deep convection days, precipitation begins from preceding afternoon,

peaks at about  $30 \text{ mm day}^{-1}$  at 0200 LST, and lasts until early morning. On fair-weather shallow cumulus days, low cloud fraction maximizes at about 10%–12% at 1.8 km from 1200 to 1400 LST. On late afternoon deep convection days, low cloud development is also found from early morning (0700 LST) to early afternoon (1400 LST), and more middle and high level clouds are present during these hours. On these days, the low cloud base gradually rises and the low cloud fraction maximizes at about 25% at 1.8 km near 1200 LST. After 1500 LST, deep convection clouds develop and peak at about 30% at 12 km between 1700 and 1800 LST and then high anvil clouds persist until midnight. Low clouds precede deep convection clouds on late afternoon deep convection days, whereas, on the contrary, high clouds precede the deep convection clouds on nighttime deep convection days and are present during the whole precipitation process. This progression of clouds on nighttime deep convection days is consistent with propagating convection that is not locally generated.

### 3. Comparing days of fair-weather shallow cumulus with days of late afternoon deep convection

As revealed by the composites, shallow cumulus clouds are present on both fair-weather and late afternoon deep convection days. By contrasting the differences in environmental parameters between these two regimes, we hope to infer what factors cause shallow convection to remain shallow on some days and to grow into deep convection on the other days. The differences between the two regimes are identified by comparing the composite mean of environmental parameters and its standard error, which is defined as the standard deviation (std dev) divided by the square root of the number of observations. We then make a two-sided Student’s  $t$

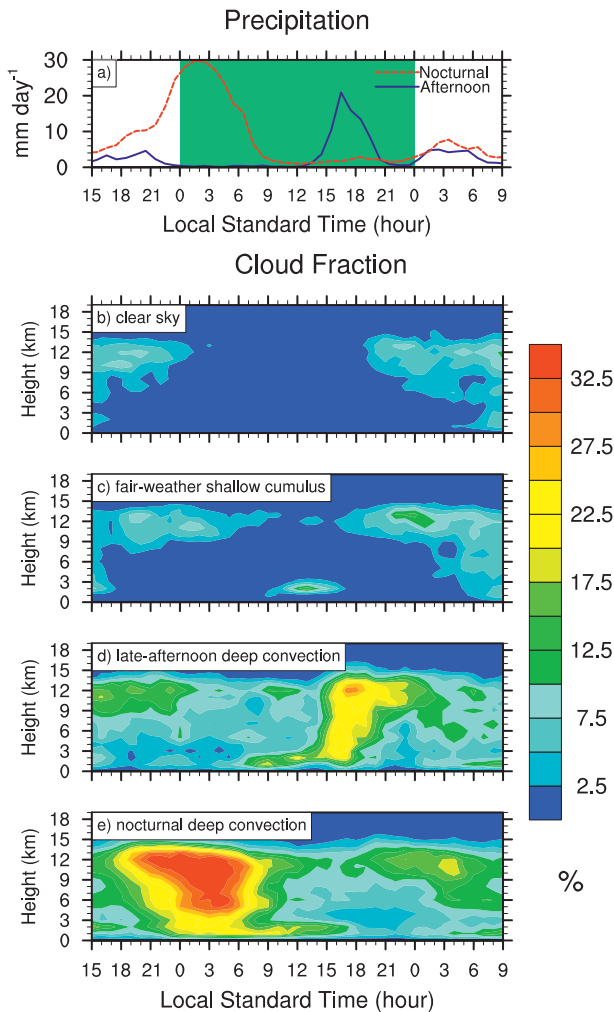


FIG. 3. Diurnal cycle composites of (a) ABRFC surface precipitation and (b)–(e) CMBE ARSCL cloud fraction for different convection regimes: (b) clear-sky days, (c) fair-weather shallow cumulus days, (d) late-afternoon deep convection days, and (e) nighttime deep convection days. In (a), the blue line denotes the precipitation rate for late-afternoon deep convection days, whereas the red line is for nighttime deep convection days; the green shaded area signifies the diurnal cycle of interest; the 9-h periods before and after are also shown for the purpose of process continuity.

test to identify which environmental parameters are the most distinguishable between the two regimes, especially around 1130 LST, the nearest sounding time before deep convection occurs.

Because balloon soundings at 1130 LST are not available every day, there are only 33 days with sounding data for late afternoon deep convection and 69 days for fair-weather shallow cumulus. For the *t* test and correlation calculations reported in the next section, only data for all parameters on valid sounding days are used, and the result is considered statistically significant only if the null hypothesis can be rejected at the 95% confidence level.

*a. Atmospheric stability: CAPE and CIN*

Figure 4 shows sounding composites in the lowest 4 km for potential temperature  $\theta$  and water vapor mixing ratio (MR) at four times: 0530, 1130, 1730, and 2330 LST. In general, a stable boundary layer is found at 0530 LST. On shallow cumulus days, a well-mixed layer is found at 1130 LST and by 1730 LST the mixed layer has deepened, warmed, and dried. At 1130 LST, deep convection days tend to have a shallower mixed layer and are slightly cooler and substantially moister than shallow cumulus days. At 1730 LST, there is a lack of well mixedness on deep convection days, which may result from the effects of precipitation on the subcloud layer. By 2330 LST, the boundary layer has returned to stable conditions for both regimes. Above 4 km, the temperature profiles of the two regimes are nearly identical (not shown), but the mixing ratio tends to be higher on deep convection days; for example, at 4 km at 1130 LST, it is  $3.5 \text{ g kg}^{-1}$  on deep convection days, which is  $1 \text{ g kg}^{-1}$  larger than that on shallow cumulus days.

The composite soundings are used to investigate atmospheric stability. Figure 4 shows the virtual temperature differences  $T_{v,d}$  between the environmental sounding and a parcel of air raised from the boundary layer;  $T_{v,d}$  is calculated by lifting an air parcel with the maximum equivalent potential temperature  $\theta_e$  between 100 and 500 m above ground through reversible adiabatic processes without mixing with the environment. Here,  $T_{v,d} > 0$  denotes positive buoyancy for the air parcel. Figure 4 shows a significant difference in the depth of the convection inhibition (CIN) layer between the two regimes. At 1130 LST, the level of free convection (LFC) for shallow cumulus days is at 4.2 km, whereas the LFC for deep convection days is at 2.5 km. The values of CAPE and CIN are  $700$  and  $40 \text{ J kg}^{-1}$ , respectively, on deep convection days but  $200$  and  $70 \text{ J kg}^{-1}$  on shallow cumulus days. At 1730 LST, there is a slight decrease from the value at 1130 LST in CIN and a large increase in CAPE on shallow cumulus days, whereas, on deep convection days, both CIN and CAPE slightly increase from 1130 to 1730 LST.

*b. Atmospheric humidity and liquid water content*

Figure 5 shows the composite sounding of relative humidity (RH) at 1130 LST and the diurnal variation of the composite PWV and LWP retrieved from the microwave radiometer. The sounding data show that more moisture is present on late afternoon deep convection days in both the boundary layer and the free troposphere. Specifically, RH is about 10% greater on deep convection days, with the largest RH differences between 2 and 4 km. Note that the majority of shallow

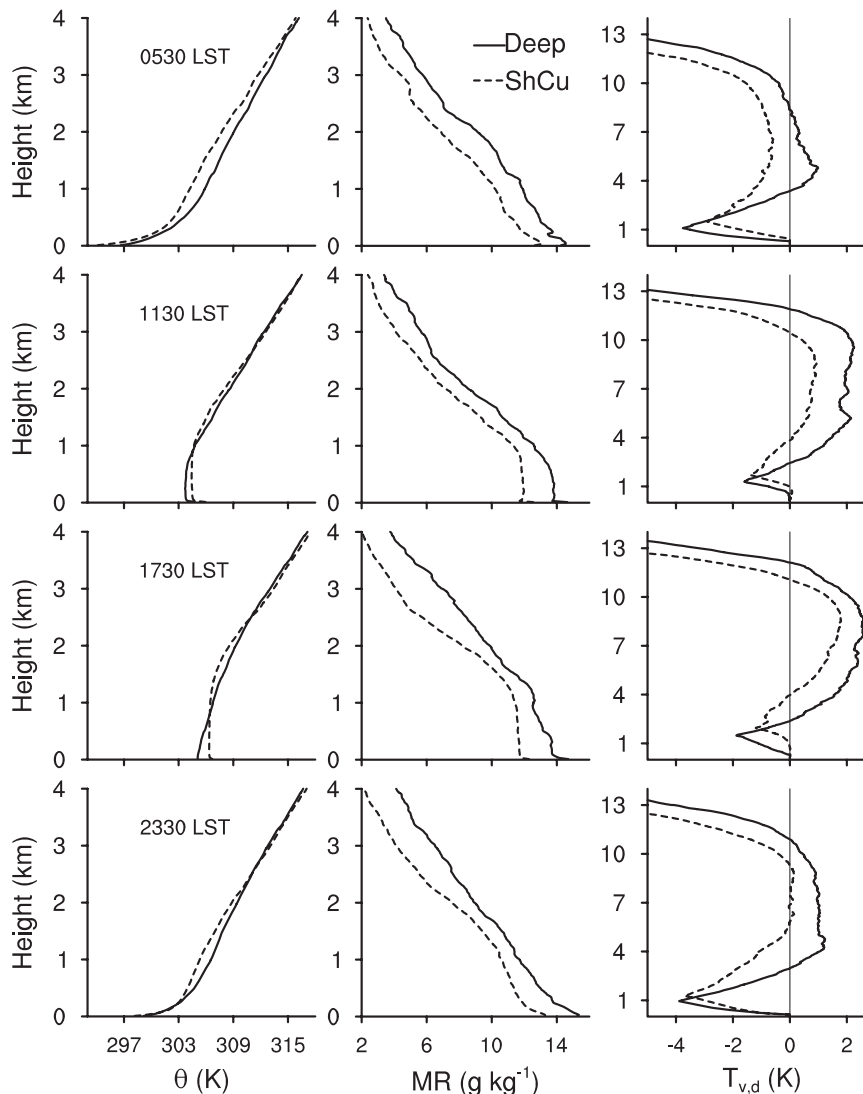


FIG. 4. Composite soundings for potential temperature  $\theta$  and MR and the virtual temperature difference  $T_{v,d}$  between the environmental sounding and an air parcel lifted through reversible adiabatic processes from the boundary layer for fair-weather shallow cumulus days (dashed) and late afternoon deep convection days (solid) at different times (LST).

cumulus is beneath the 2.5-km level at 1130 LST for both regimes, indicating that the extra moisture in this layer is unlikely to be the result of moistening by cumulus clouds on the same day. The moisture difference is also apparent in PWV and LWP, both of which are significantly larger on days with afternoon deep convection. The PWV shows a strong diurnal cycle with an increase of about 5 mm from sunrise to its afternoon maximum. This average increase is larger than the average accumulated evaporation minus precipitation from the surface, suggesting that there is horizontal convergence of water vapor on days with afternoon deep convection. The afternoon peak of LWP of  $110 \text{ g m}^{-2}$  is in phase with the

peak precipitation at 1730 LST, whereas the peak LWP on shallow cumulus days is  $15 \text{ g m}^{-2}$  at 1330 LST.

### c. Surface turbulent fluxes

Figure 6 shows that the diurnal composites of surface sensible and latent heat fluxes are in phase with the solar radiation. Because the diurnal variation in surface heat fluxes drives the growth of the boundary layer, one might expect that greater surface fluxes would favor an increased chance of deep convection. However, surface heat fluxes on deep convection days are lower than those on shallow cumulus days, particularly the latent heat flux. The reduced latent heat flux may be a response to

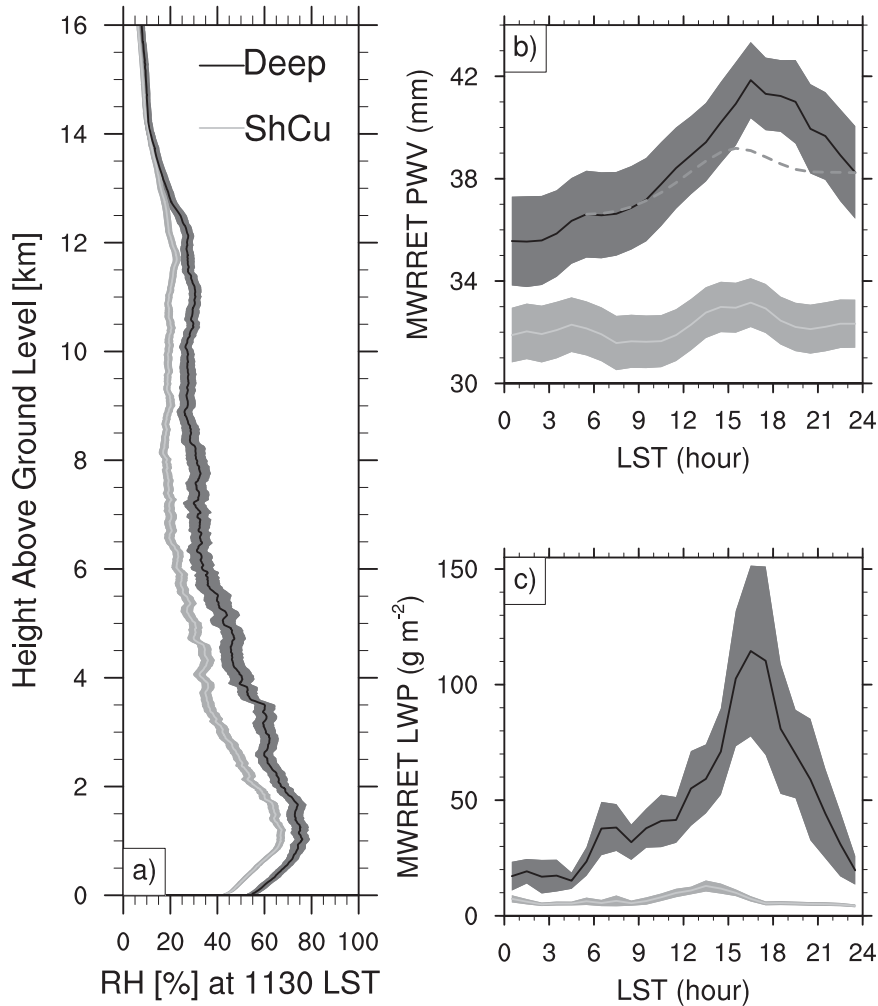


FIG. 5. (a) Composite RH at 1130 LST from sounding data and composite diurnal cycle of (b) PWV and (c) LWP from CMBE MWRRET data. The width of the shading on either side of the mean value denotes one standard error of the mean across all the sample days in each regime. The dashed line in (b) is the PWV calculated based on the integral of evaporation and precipitation, since 0530 LST for days with late afternoon deep convection. Time-averaged LWP values are not conditioned on the presence of cloud, and thus they are not in-cloud averages.

boundary layer moisture. Specifically, the increase in near-surface relative humidity from 45% on shallow cumulus days to 55% on deep convection days at 1130 LST (Fig. 5) reduces the potential for evaporation and transpiration on deep convection days. The sensible heat fluxes are only distinguishable between 1330 and 1800 LST; the lower value on days with afternoon deep convection may be related to the reduced solar radiative heating of the surface (not shown). We also note that this association of reduced surface fluxes with deep convection may be similar to that found over tropical oceans, because deep convection there is usually associated with moisture convergence and a minimum in surface fluxes (Sobel 2003).

*d. Boundary layer inhomogeneity*

To investigate boundary layer inhomogeneity, we use surface wind, temperature and humidity data measured by the SMOS at the central facility and four surrounding Oklahoma Mesonet stations (Fig. 1). Figure 7 shows the diurnal cycle of the mean and std dev of the surface moist static energy (MSE), temperature, water vapor mixing ratio, and horizontal wind speed across the five stations. The mesoscale wind (wind std dev) is defined as  $\sqrt{u'^2 + v'^2}$ , where  $u'$  and  $v'$  are the deviations in zonal and meridional wind from the five-station mean. Note that we feel justified using the term mesoscale to define variability across the domain as the individual data at

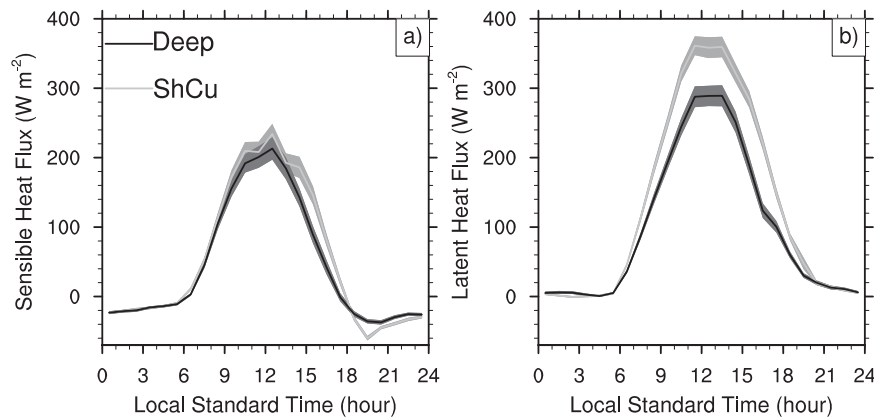


FIG. 6. Diurnal cycle composite of (a) surface sensible heat flux and (b) latent heat flux from BAEBBR data for fair-weather shallow cumulus days and late afternoon deep convection days. The width of the shading on either side of the mean value denotes one standard error of the mean across all the sample days in each regime.

each station are 60-min averages, which correspond to a distance of 18 km for a  $5 \text{ m s}^{-1}$  horizontal wind speed. The mean MSE on deep convection days peaks in early afternoon around 1400 LST, whereas that on shallow cumulus days maximizes in the last morning around 1100 LST. For both regimes, a quick increase of mixing ratio occurs in the early morning from 0600 to 0900 LST. After 0900 LST, the moisture on deep convection days stabilizes, whereas the moisture on shallow cumulus days markedly decreases until sunset. The mean temperature difference is distinguishable between regimes only in the late afternoon and early evening. The mean daytime surface wind speed on shallow cumulus days is slightly larger than that on deep convection days.

The variations in MSE, mixing ratio and wind speed across the domain become significantly larger on deep convection days after 1330 LST, when precipitation starts to pick up. Although temperature variability is already larger on the morning of deep convection days, its significant increase occurs after 1330 LST. Broadly speaking, the station data clearly show that boundary layer inhomogeneity is significantly larger on deep convection days from near precipitation onset through early evening and beyond.

#### e. Large-scale wind fields

Figure 8 shows composites of horizontal and vertical winds from NCEP MOLTS data. Beneath 850 hPa, the horizontal wind fields are quite similar for both regimes. The wind direction is southwesterly before noon and turns to southeasterly in the afternoon and evening. Southerly winds prevail and become stronger during nighttime consistent with the existence of a low-level jet (Stensrud 1996).

The differences in horizontal winds between the two regimes are found at higher levels. Southerly winds extend into the middle and upper troposphere on deep convection days, whereas the southerly component of the wind is near zero on shallow cumulus days, especially during daytime. Although the westerly components of upper-level winds are stronger on deep convection days, the differences in westerly winds between the two regimes at middle and low levels are not large. The southerly winds immediately above the boundary layer on deep convection days could bring moister air from southerly locations, leading to the greater humidity above the boundary layer.

To explore this idea, we correlate wind data at levels between 600 and 850 hPa with PWV from MWRRET. PWV varies with wind direction in the 600–850-hPa layer, because PWV with southerly winds is 20% higher than it is with northerly winds, whereas PWV does not differentiate between easterly and westerly winds. Although 60% of shallow cumulus days have southerly winds in the 600–850-hPa layer around 1130 LST, more than 80% of deep convection days have southerly winds in this layer. However, the magnitude of southerly winds does not seem to matter, because no significant correlation is found between the meridional wind in the 600–850-hPa layer and PWV. This suggests wind direction, rather than wind speed, is more important for moisture in this layer.

With respect to large-scale vertical velocity, subsidence is found between 200 and 850 hPa on shallow cumulus days with an early afternoon maximum. Subsidence is also present around 600 hPa from 0900 to 1500 LST on late afternoon deep convection days, but with much reduced magnitude. In general, the subsidence is greatly reduced at all levels on deep convection days relative to that on shallow cumulus days.

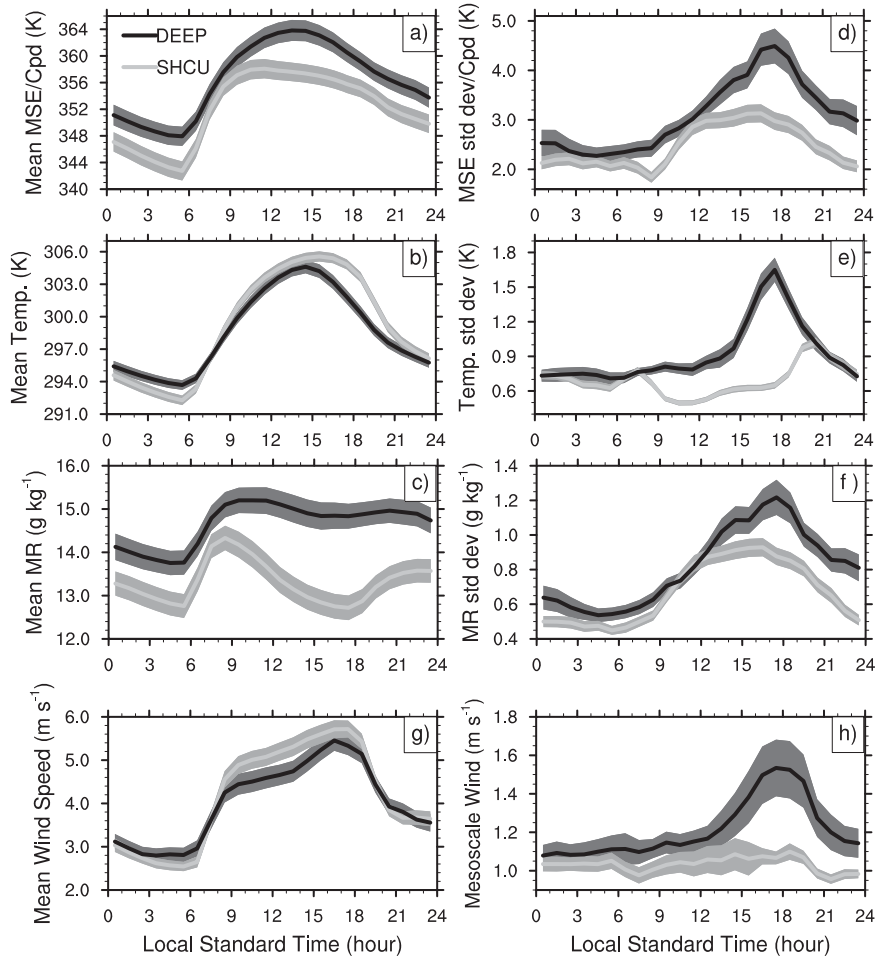


FIG. 7. Diurnal cycle composite of (a) mean surface MSE, (b) temperature, (c) and MR and (d)–(f) their std dev. Also shown are (g) the mean surface wind speed and (h) the mesoscale wind speed. Mean and std dev values are calculated based on SMOS data at the SGP CF and four nearby Oklahoma Mesonet stations. Mean MSE and its std dev are normalized by the heat capacity at constant pressure for dry air (Cpd) and thus are in units of K. The width of the shading on either side of the mean value denotes one standard error of the mean value across all sample days in each regime.

*f. What is the most different?*

Figure 9 records *t*-test values and significance levels for a set of environmental parameters at 1130 LST in the order of a decreasing *t*-test value. Note that we examined differences at this time, because this is the nearest time before the transition when soundings are available and because values of environmental parameters before the transition may indicate which factors are important for the transition.

The definitions of various environmental parameters are as follows: RH is calculated as the ratio of actual PWV to saturated PWV between 2 and 4 km and in the mixed layer. The NCEP winds are calculated between levels of 600 and 850 hPa, roughly corresponding to 1.2–4 km above ground level. These levels are examined because

they correspond to CIN layers suggested by Fig. 4. Here,  $-dT/dz$  is the temperature lapse rate between 2 and 4 km. CAPE and CIN are calculated from sounding profiles of temperature and humidity at 1130 LST. For an individual sounding, the buoyancy profile ( $T_{v,d}$  in Fig. 4) might cross the zero line several times. Because such complexity might lead to ambiguity in determining CAPE and CIN, we introduce an additional buoyancy parameter, the average undilute buoyancy regardless of sign below 5 km, to roughly measure the ability of a boundary layer air parcel originating from the mixed layer to reach the level of free convection. Other environmental parameters are averages between 1030 and 1230 LST.

The results indicate the RH between 2 and 4 km at 1130 LST has the greatest statistical significance of all

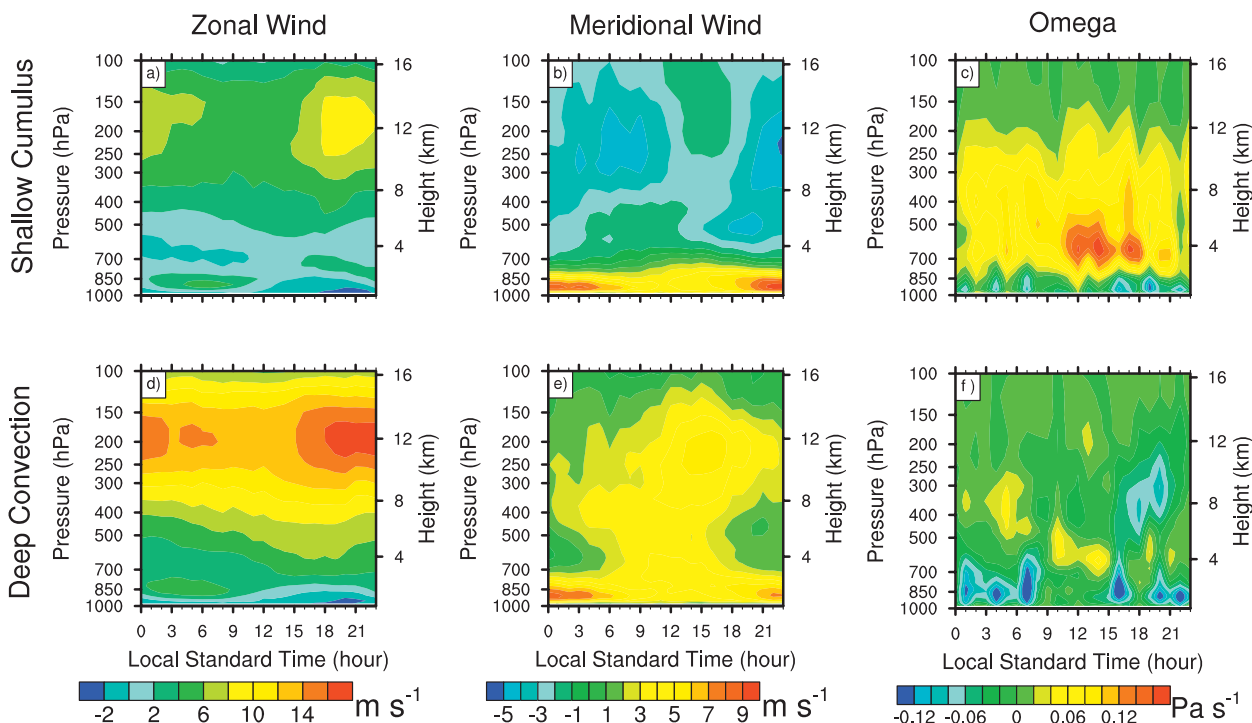


FIG. 8. Composite diurnal cycle of winds from the NCEP MOLTS data at SGP: (left) zonal, (middle) meridional, and (right) vertical pressure wind (omega) for (top) fair-weather shallow cumulus days and (bottom) late afternoon deep convection days.

these environmental parameters. This supports the role of free-tropospheric humidity in influencing the transition from shallow cumulus to deep convection. Smaller latent heat flux and stronger 600–850-hPa southerly wind hint that moisture may be not only from surface evaporation and that southerly winds play an important role in moisture transfer into the SGP region. At 1130 LST, a larger temperature standard deviation is found on deep convection days, whereas the differences in MSE and moisture standard deviations are not significant. The differences in these standard deviations are significant at later hours of the day. CAPE and CIN are not significantly different between the two regimes at the 95% confidence level, which is possibly because of the noise introduced by the complexity of buoyancy profiles in individual soundings. However, other measures of stability such as average buoyancy below 5 km and 2–4 km  $-dT/dz$  are found to be significantly larger on deep convection days.

#### 4. Comparing afternoon rain statistics with environmental parameters

An alternate technique to determine the factors that favor the transition is to examine how rain statistics vary with environmental parameters only on the days with late afternoon deep convection. In particular, we ask, is there any correlation between environmental parameters

and rain statistics on days with late afternoon deep convection? The rain statistics consist of four characteristics: total rain amount, the maximum hourly rain rate, the duration of a rain event, and the precipitation onset time. The onset time is defined as when the precipitation rate first exceeds  $0 \text{ mm day}^{-1}$  at or after 1130 LST. Testing of the onset time with the precipitation rate first exceeding  $1 \text{ mm day}^{-1}$  also yields similar results.

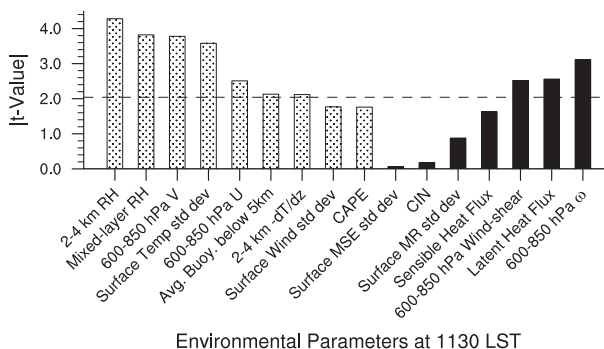


FIG. 9. Absolute values from Student's  $t$  tests for the differences between composite means of fair-weather shallow cumulus days and late-afternoon deep convection days around 1130 LST. The horizontal line denotes a confidence level of 95%. Negative (positive) values are in solid (stippled) pattern and denote smaller (larger) composite means on deep convection days relative to the mean on fair-weather shallow cumulus days.

TABLE 1. Correlation coefficients between environmental parameters at 1130 LST and afternoon rain statistics. Correlation coefficients are shown only if the relationship is significant at the 95% confidence level.

	Tot rain	Max rain rate	Onset time	Duration
CAPE			0.414	-0.417
CIN				
Avg buoyancy below 5 km				
2–4-km $-dT/dZ$	0.496	0.518		
2–4-km RH			-0.395	0.464
Mixed layer RH				
Surface MSE std dev	0.437	0.513		
Surface MR std dev	0.443	0.492		
Surface temperature std dev	0.550	0.552		
Surface mesoscale wind	0.514	0.486		
Sensible heat flux				
Latent heat flux				-0.436
600–850-hPa wind shear				
600–850-hPa $\omega$				
600–850-hPa $U$	0.454	0.549		
600–850-hPa $V$				

*a. What is best correlated to afternoon rain?*

Table 1 displays the correlation coefficients between afternoon rain statistics and environmental parameters at 1130 LST. The results indicate that larger RH between 2 and 4 km leads to earlier onset time and longer duration of precipitation. Total rain amount and maximum rain rate are positively correlated with the lapse rate between 2 and 4 km, boundary layer inhomogeneity in wind, temperature and humidity, and 600–850-hPa westerly wind. Although the signs of these significant correlation coefficients match expectations, some parameters are correlated to the rain statistics in a way contrary to expectation. For example, larger CAPE is correlated with a later onset time and shorter duration of precipitation. A larger surface latent heat flux is related to a shorter duration of precipitation, which hints that the flux is a response to a drier boundary layer.

We note that some environmental parameters show no statistically significant correlation with the rain statistics, although they are found significantly different between the two regimes in the  $t$  test. These include mixed layer RH, the magnitude of the southerly wind component between 600 and 850 hPa, the average buoyancy below 5 km of an undilute surface air parcel, and large-scale vertical velocity. Furthermore, some environmental parameters are correlated with the rain statistics, even though they are not significantly different in the  $t$  test. These include CAPE and boundary layer variability in MSE, mixing ratio, and wind speed. These facts remind us that there might be limitations in both the  $t$  test and this correlation test. For example, the results are sensitive to the choices of the measures, because CAPE, CIN, average buoyancy below 5 km, and 2–4 km  $-dT/dz$  each represent different aspects of

atmospheric stability and show different behavior in the tests. Furthermore, the convection process is nonlinear and might be sensitive to a threshold value in some environmental parameters. As long as it is above a threshold, deep convection would be triggered and the actual magnitude of the environmental parameters might not be as important. In addition, because deep convection might occur sooner or later in the afternoon, using a fixed sounding time at 1130 LST might mix some signals in the environmental parameters at different stages relative to the triggering of convection. More detailed checks on the relationships in Table 1 are discussed in the following subsections.

Cross correlations among environmental parameters are examined to identify redundant environmental parameters (not shown). The surprising correlation of rain statistics to the westerly wind between 600 and 850 hPa is partially explained by the fact that the westerly wind is positively correlated to both 2–4-km lapse rate and boundary layer temperature variability. Furthermore, the fact that both 2–4-km RH and boundary layer moisture variability are positively related to (albeit different) rain statistics in Table 1 is striking, given that greater 2–4-km RH is correlated significantly with smaller boundary layer moisture variability. Other environmental parameters have no significant correlations among each other and thus appear to be potentially independent predictors of afternoon rain statistics.

*b. The relationship of sounding parameters to afternoon rain statistics*

To provide an illustration of these relationships, we present Fig. 10, which stratifies the rain statistics according to the two 1130 LST sounding parameters, 2–4-km RH and  $-dT/dz$ , which show the strongest relationship to

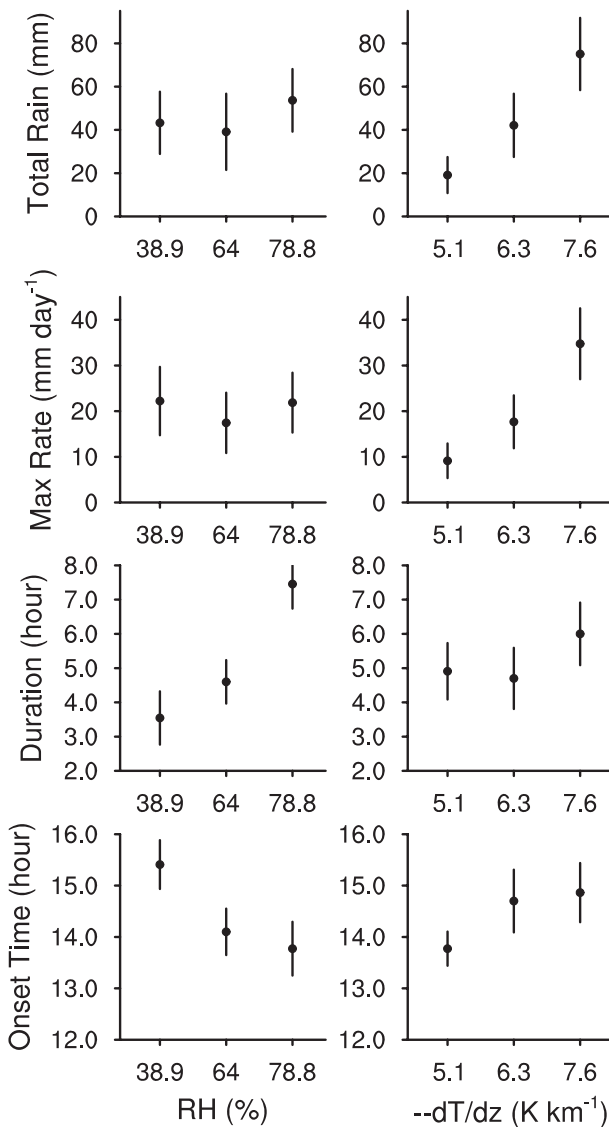


FIG. 10. Afternoon rain statistics stratified according to low, medium, and high values of RH and lapse rate  $-dT/dz$  between 2 and 4 km at 1130 LST. The statistics include (top to bottom) total afternoon rain, maximum hourly rain rate, duration of rain event, and precipitation onset time. The black dots indicate the mean values of precipitation statistics, and the width of the black lines indicates two standard errors. The mean values for each of the three ranges of RH and lapse rate are displayed on the abscissa.

afternoon rain. The 33 soundings at 1130 LST are sorted into three groups of 11 according to whether they have low, medium, or high values of the sounding parameter. The mean and the standard error of each rain statistic are calculated from the 11 samples in each group. Figure 10 shows that total rain amount and maximum rain rate do not distinguish among different 2–4-km RHs. However, with larger RH, the rain tends to start earlier and last

longer. The quicker onset with larger RH is in agreement with Kuang and Bretherton (2006), who found in their LES that the transition is accelerated by a more humid free troposphere. The analysis for the 2–4-km temperature lapse rate  $-dT/dz$  shows that more unstable conditions are associated with larger total rain amount and maximum rain rate. Surprisingly, more unstable conditions are associated with a later precipitation onset time, contrary to the modeling results of Wu et al. (2009) and Houston and Niyogi (2007).

### c. The relationship of boundary layer inhomogeneity to afternoon rain statistics

Because of its hourly record, our analysis of the relationship of rain statistics to boundary layer inhomogeneity need not be restricted to the values at 1130 LST. Furthermore, because boundary layer inhomogeneity can be both the cause and result of deep convection, high-frequency data are necessary to discern cause and effect. To this end, we calculate the time-lag correlation coefficients between boundary layer inhomogeneity and the hourly precipitation rate. In performing this calculation, we align the time series data for each precipitation event with respect to the precipitation onset time. By so doing, we try to avoid mixing different development stages of deep convection.

Our results are illustrated with the matrix of lead-lag correlation coefficients in time relative to precipitation onset (Fig. 11). The simultaneous correlation between inhomogeneity and precipitation is shown on the diagonal line (black solid line in Fig. 11); the correlation coefficients for inhomogeneity leading (following) precipitation are shown in the bottom-right (top left) part of the plot. For example, the correlation coefficient of moist static energy standard deviation 2 h before precipitation begins with the precipitation rate 2 h after precipitation begins is plotted at abscissa and ordinate location (2, -2) in Fig. 11a.

The most significant correlations of precipitation appear with temperature variability and mesoscale wind speeds. Particularly prominent is a correlation coefficient of 0.7, the highest reported in this paper, between temperature variability and precipitation 3 h after precipitation onset. The fact that the strongest correlations are along the diagonal line suggests that the time scale for precipitation to create boundary layer variability or vice versa must be fast and less than an hour. Although cause and effect may therefore be difficult to discern even with hourly data, a closer inspection of Fig. 11b shows that, during the first 2 h after precipitation onset, the strongest correlation in each column is for precipitation leading temperature or wind variability by 1 h. This hints that temperature or wind variability is the result of precipitation, at least early in a precipitation event.

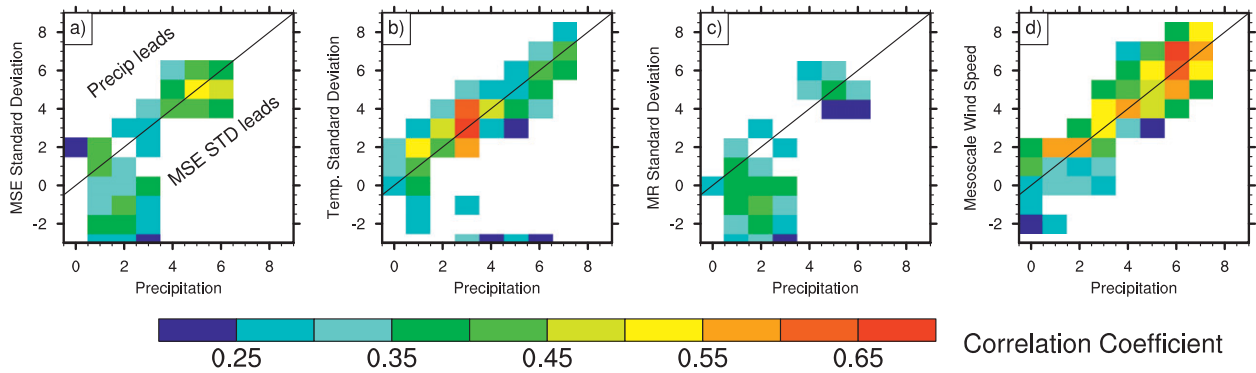


FIG. 11. Lead-lag correlation coefficients between the precipitation rate of late afternoon deep convection days and the std dev of (a) surface MSE, (b) surface temperature, (c) surface MR, and (d) mesoscale wind speed. The scale for both the abscissa and ordinate are hours after precipitation onset time. Only correlation coefficients significant at 95% confidence level and that have been calculated from samples sizes >30 are displayed.

The opposite relationship is suggested by the correlation at a level of 0.4 between the surface moisture variability 1–3 h before the onset of precipitation and the precipitation rate 1–3 h after the onset. This hints that surface moisture variability leads and therefore might enhance precipitation during the initial stage of a rain event.

**5. Discussion**

The calculations of sections 3 and 4 both suggest that lower-tropospheric humidity and boundary layer inhomogeneity play important roles in the transition from shallow to deep convection. In this section, we use a Paluch diagram (Fig. 12) for conservative thermodynamic variables (Paluch 1979; Neggers et al. 2002; Wu et al. 2009) to provide an interpretation of our results. In this diagram, an air parcel will preserve its thermodynamic properties (total water mixing ratio  $q_t$  and liquid water potential temperature  $\theta_l$ ) if it is lifted adiabatically without mixing with its environment. The properties of mixtures of boundary layer and environmental air would fall along the mixing line that connects the original air parcel properties in boundary layer with the properties of the environment at our chosen level. We select 2.5 km for this level, because it is the level of free convection on deep convection days (Fig. 4).

Figure 12 shows that, on deep convection days at 1130 LST, almost all cloud properties including the average are negatively buoyant. The exception is for the undilute boundary layer air property, which is barely positively buoyant. Thus, it is consistent with the fact that deep convection has not begun at 1130 LST. Because we do not have soundings at 1430 LST, which is the mean time of transition to deep convection, we can only estimate the change in boundary layer air property

based on the changes in surface temperature and moisture in Fig. 7 and with the assumption that the change in air properties at 2.5 km is small based on Fig. 4. In this case, the undiluted boundary layer air is significantly positive buoyant and the average cloud property barely makes it to the zero-buoyancy line on deep convection days, whereas the same quantities on shallow cumulus days are both negatively buoyant. Indeed, it is striking that undiluted boundary layer air on shallow cumulus days is no closer to the zero-buoyancy line at 1430 LST despite being 2 K warmer relative to the value at 1130 LST. This is due to the drying of the boundary layer in these 3 h, which itself is likely the result of entrainment of relatively dry free-tropospheric air into the boundary layer on these days.

It is also interesting to note that temperature differences between two regimes are small above the boundary layer (Fig. 4). As a result, the difference between the two regimes in the zero-buoyancy lines decreases with height and is small relative to the separation between the two regimes in soundings and mixing lines. This means that it is the higher moisture both in and above the boundary layer that is the main reason leading to greater buoyancy on deep convection days for both an undilute air parcel and the average cloud property estimated from a mixing line.

Figure 12 also shows the possible values of boundary layer air properties at 1430 LST if the inhomogeneity in both temperature and moisture are considered based on Fig. 7. Note that boundary layer inhomogeneity in Fig. 7 represents mesoscale variability and thus is an underestimate of air parcel (~1 km) variability. It is obvious that, in a certain range of combined variability in temperature and moisture, the buoyancy of an undilute air parcel or the average cloud property will increase positively. Furthermore, the Paluch diagram provides

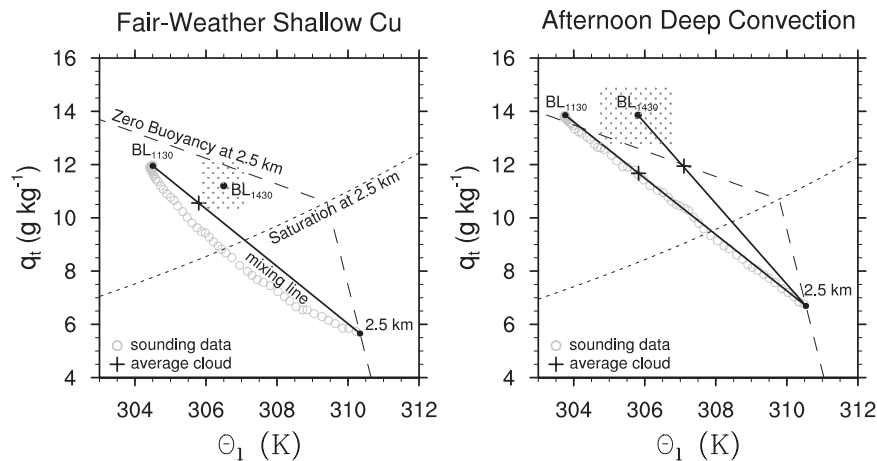


FIG. 12. Conservative variables diagram (Paluch diagram) of total water MR  $q_t$  and liquid water potential temperature  $\theta_l$  for the composite of sounding data (gray dots) at 1130 LST for (left) fair-weather shallow cumulus days and (right) late-afternoon deep convection days. Dotted lines are the saturation curves and long-dashed lines are the zero-buoyancy lines calculated based on sounding data at 2.5 km. The black solid line connects the air properties in the boundary layer at 1130 LST (black dot labeled  $\text{BL}_{1130}$ ) and at the level of 2.5 km (black dot labeled 2.5 km) and is the mixing line along which mixtures of air in boundary layer and the 2.5-km level would fall. The portion of the mixing line above the zero-buoyancy line indicates mixture is positively buoyant at 2.5 km. Above the saturation curve, the mixture is cloudy at 2.5 km. The black crosses denote the average property of the mixing line above the saturation curve, which is an approximation to the average properties of the cloud at 2.5 km. The boundary layer air property at 1430 LST is denoted by the black dot labeled  $\text{BL}_{1430}$ . The stippled area denotes the possible values a boundary layer air parcel may have if boundary layer inhomogeneity is considered. This area encompasses 1 std dev of boundary layer inhomogeneity about the mean value (Fig. 7).

a means to understand why moisture variability may lead the precipitation by a few hours in the early stages of a precipitation event (Fig. 11) and yet there is no distinguishable difference in moisture variability between shallow cumulus and deep convection days at 1130 LST (Fig. 9). Specifically, the effect of a given temperature or moisture variability is larger on deep convection days than it is on shallow cumulus days, because mixtures are closer to neutral buoyancy on deep convection days than they are on shallow cumulus days.

Nonetheless, the causes of boundary layer inhomogeneity before afternoon deep convection begins are unclear. Temperature variability at 1130 LST on deep convection days is 0.3 K larger than the variability on shallow cumulus days (Fig. 7). One possibility is that the larger surface solar cloud radiative effect on deep convection days may induce greater mesoscale temperature variability. Note that the low cloud fraction on deep convection days is nearly double the value on shallow cumulus days (Fig. 3).

Although thermodynamic conditions may explain the difference between regimes, one must still ask, how does an air parcel reach the level of free convection? This

leads us to consider the role of surface fluxes and boundary layer inhomogeneity in creating the momentum to overcome the CIN layer. Traditionally, the vertical velocity of air parcel in the boundary layer can be characterized by the convective velocity scale  $w_*$ , which we can calculate from the observed surface fluxes and mixed layer depth. We find that  $w_*^2$  is about  $1.4^2 \text{ J kg}^{-1}$  for deep convection days and  $1.7^2 \text{ J kg}^{-1}$  for shallow cumulus days at 1130 LST. These kinetic energy values are small relevant to the CIN present at 1130 LST. However, the CIN at transition time may be considerably smaller and mesoscale fluctuations in wind speed that are larger on deep convection days (Fig. 7) may contribute additional momentum that could increase the chances for shallow cumulus to transit to deep convection.

## 6. Summary and implications for convection parameterization

Summertime observations for 11 yr at the ARM Southern Great Plains site have been used to categorize the diurnal cycle into different convection regimes based on the diurnal variation of precipitation and clouds. We

focus on the comparison of environmental parameters between two regimes, the days with fair-weather shallow cumulus and the days with afternoon deep convection, to reveal the mechanisms controlling the transition from shallow to deep convection.

A few hours before rain events begin on afternoon deep convection days, higher relative humidity is found both in and above the boundary layer, especially between the levels of 2 and 4 km above the surface. The higher moisture content at 2–4 km depends on the wind direction being from the south. Relative to days of fair-weather shallow cumulus, greater instability, stronger inhomogeneity in boundary layer temperature, less wind shear between 600 and 850 hPa, and weaker subsidence are found preceding afternoon rain events. Based on the composite sounding for the two regimes, we also find that the level of free convection is 1.7 km lower on days with afternoon rain events. Furthermore, although the diurnal variation in surface fluxes drives the growth of the boundary layer, the difference between regimes in their magnitude appears to be a response to changed boundary layer conditions.

We then focused on the relationship between these conditions at 1130 LST and afternoon rain statistics. Four afternoon rain properties, the total rain amount, maximum hourly rain rate, rain onset time, and duration of rain were investigated. With greater 2–4-km relative humidity, rain starts earlier and lasts longer. Boundary layer inhomogeneity, 600–850-hPa westerly wind component, and the 2–4-km lapse rate are positively correlated with total rain and maximum rain rate; furthermore, these environmental parameters are correlated with each other.

Although not manifest in every statistical test, these observations are consistent with a role for lower-tropospheric (2–4 km) humidity and boundary layer inhomogeneity in the transition from shallow to deep convection. This provides some observational support for the transition theories based on LES and is consistent with previous observations that have focused mainly on tropical ocean deep convection. With respect to boundary layer variability, we showed that in the early stage of precipitation, boundary layer temperature and wind variability slightly lags precipitation by up to 1 h (Figs. 12b,d). The creation of cold pools by deep convection may explain this correlation as well as the large increase of boundary layer inhomogeneity on deep convection days relative to that on shallow cumulus days. In addition, we also showed a connection between moisture and moist static energy inhomogeneity before afternoon precipitation begins and the subsequent precipitation (Figs. 12a,c and Table 1). This last correlation suggests that boundary layer inhomogeneity promotes as well as results from deep convection. Note, however, that the

inhomogeneity that may promote convection is not due to cold pools, because this is the inhomogeneity present before precipitation. The reason we do not observe cold pools promoting convection may be that this effect is masked by the more dominant effect of convection causing cold pools. To observe the effect of cold pools promoting convection may require alternate observational techniques such as a detailed analysis of individual events using the new scanning Doppler cloud radars and lidars currently being installed by ARM at the Southern Great Plains site.

A plausible, albeit not exclusive, interpretation is that the observational evidence is consistent with a mechanistic view of the transition from shallow to deep convection that emphasizes the ability of a parcel of boundary layer air to reach the level of free convection. In particular, the parcels that reach the level of free convection are those that have the highest values of moisture in the boundary layer, and they may have more momentum than expected because of mesoscale fluctuations in boundary layer wind. The ability of the “lucky” parcels to reach the level of free convection is also assisted by high relative humidity and a steeper lapse rate in the first few kilometers above the boundary layer. Higher relative humidity in this layer diminishes the buoyancy-reducing effects of entrainment, whereas the steeper lapse rate increases parcel buoyancy directly. Therefore, these observations provide partial support to parameterizations focusing on the ability of boundary layer air parcel to penetrate level of free convection, similar to the evolving CIN-based parameterizations of moist convection that have been under development for a number of years (Mapes 2000; Bretherton et al. 2004a; Fletcher and Bretherton 2010). Furthermore, the observations are somewhat encouraging for the nascent efforts to parameterize mesoscale boundary layer inhomogeneity (Rio et al. 2009) and its role in the transition from shallow to deep convection.

*Acknowledgments.* The authors sincerely thank Larry Berg for providing the index for shallow cumulus days, Shaocheng Xie for providing codes to calculate CAPE and CIN, and Renata McCoy for discussions on the CMBE data. The authors thank Brian Mapes, Peter Caldwell, and Shaocheng Xie for comments on the manuscript and Bjorn Stevens, Chris Bretherton, and Robert Pincus for discussions. The authors also appreciate the comments of three anonymous reviewers, which helped to improve the manuscript. Data from the U.S. Department of Energy as part of the Atmospheric Radiation Measurement (ARM) Climate Research Facility Southern Great Plains site were used. The Oklahoma Mesonet data were used. This work was supported primarily by the

U.S. Department of Energy's Atmospheric System Research, an Office of Science, Office of Biological and Environmental Research program; Lawrence Livermore National Laboratory is operated for the DOE by Lawrence Livermore National Security, LLC under Contract DE-AC52-07NA27344.

## REFERENCES

- Ackerman, T. P., and G. M. Stokes, 2003: The Atmospheric Radiation Measurement program. *Phys. Today*, **56**, 38–44.
- Arakawa, A., and W. H. Schubert, 1974: Interaction of a cumulus cloud ensemble with the large-scale environment, part I. *J. Atmos. Sci.*, **31**, 674–701.
- Bechtold, P., J.-P. Chaboureaud, A. Beljaars, A. K. Betts, M. Köhler, M. Miller, and J.-L. Redelsperger, 2004: The simulation of the diurnal cycle of convective precipitation over land in a global model. *Quart. J. Roy. Meteor. Soc.*, **130**, 3119–3137.
- Berg, L. K., and E. I. Kassianov, 2008: Temporal variability of fair-weather cumulus statistics at the ACRF SGP site. *J. Climate*, **21**, 3344–3358.
- Breidenbach, J., D. J. Seo, and R. Fulton, 1998: Stage II and III post processing of NEXRAD precipitation estimates in the modernized weather service. Preprints, *14th Int. Conf. on Interactive Information and Processing Systems for Meteorology, Oceanography, and Hydrology*, Phoenix, AZ, Amer. Meteor. Soc., 263–266.
- Bretherton, C. S., J. R. McCaa, and H. Grenier, 2004a: A new parameterization for shallow cumulus convection and its application to marine shallow subtropical cloud-topped boundary layers. Part I: Description and 1D results. *Mon. Wea. Rev.*, **132**, 864–882.
- , M. E. Peters, and L. E. Back, 2004b: Relationships between water vapor path and precipitation over the tropical oceans. *J. Climate*, **17**, 1517–1528.
- Brock, F. V., K. C. Crawford, R. L. Elliott, G. W. Cuperus, S. J. Stadler, H. L. Johnson, and M. D. Eilts, 1995: The Oklahoma Mesonet: A technical overview. *J. Atmos. Oceanic Technol.*, **12**, 5–19.
- Carbone, R. E., J. D. Tuttle, D. A. Ahijevych, and S. B. Trier, 2002: Inferences of predictability associated with warm season precipitation episodes. *J. Atmos. Sci.*, **59**, 2033–2056.
- Chaboureaud, J.-P., F. Guichard, J.-L. Redelsperger, and J.-P. Lafore, 2004: The role of stability and moisture in the diurnal cycle of convection over land. *Quart. J. Roy. Meteor. Soc.*, **130**, 3105–3117.
- Clothiaux, E. E., T. P. Ackerman, G. G. Mace, K. P. Moran, R. T. Marchand, M. Miller, and B. E. Martner, 2000: Objective determination of cloud heights and radar reflectivities using a combination of active remote sensors at the ARM CART sites. *J. Appl. Meteor.*, **39**, 645–665.
- , and Coauthors, 2001: The ARM millimeter wave cloud radars (MMCRs) and the active remote sensing of clouds (ARSCL) value added product (VAP). U.S. Department of Energy Tech. Memo. ARM VAP-002.1, 56 pp.
- Dai, A., 2001: Global precipitation and thunderstorm frequencies. Part II: Diurnal variations. *J. Climate*, **14**, 1112–1128.
- , 2006: Precipitation characteristics in eighteen coupled climate models. *J. Climate*, **19**, 4605–4630.
- , F. Giorgi, and K. Trenberth, 1999: Observed and model-simulated diurnal cycles of precipitation over the contiguous United States. *J. Geophys. Res.*, **104**, 6377–6402.
- Derbyshire, S. H., I. Beau, P. Bechtold, J.-Y. Grandpeix, J.-M. Piriou, J.-L. Redelsperger, and P. M. M. Soares, 2004: Sensitivity of moist convection to environmental humidity. *Quart. J. Roy. Meteor. Soc.*, **130**, 3055–3079.
- Dong, X., P. Minnis, and B. Xi, 2005: A climatology of midlatitude continental clouds from the ARM SGP Central Facility. Part I: Low-level cloud macrophysical, microphysical, and radiative properties. *J. Climate*, **18**, 1391–1410.
- Engerer, N. A., and D. J. Stensrud, 2008: Surface characteristics of observed cold pools. *Mon. Wea. Rev.*, **136**, 4839–4849.
- Fletcher, J. K., and C. S. Bretherton, 2010: Evaluating boundary layer-based mass-flux closures using cloud-resolving model simulations of deep convection. *J. Atmos. Sci.*, **67**, 2212–2225.
- Fulton, R. A., J. P. Breidenbach, D.-J. Seo, D. A. Miller, and T. O'Bannon, 1998: The WSR-88D rainfall algorithm. *Wea. Forecasting*, **13**, 377–395.
- Guichard, F., and Coauthors, 2004: Modeling the diurnal cycle of deep precipitating convection over land with cloud-resolving models and single-column models. *Quart. J. Roy. Meteor. Soc.*, **130**, 3139–3172.
- Holloway, C., and J. Neelin, 2009: Moisture vertical structure, column water vapor, and tropical deep convection. *J. Atmos. Sci.*, **66**, 1665–1683.
- Houston, A. L., and D. Niyogi, 2007: The sensitivity of convective initiation to the lapse rate of the active cloud-bearing layer. *Mon. Wea. Rev.*, **135**, 3013–3032.
- Jiang, X., N.-C. Lau, and S. A. Klein, 2006: Role of eastward propagating convection systems in the diurnal cycle and seasonal mean of summertime rainfall over the U.S. Great Plains. *Geophys. Res. Lett.*, **33**, L19809, doi:10.1029/2006GL027022.
- Khairoutdinov, M. F., and D. A. Randall, 2006: High-resolution simulation of shallow-to-deep convection transition over land. *J. Atmos. Sci.*, **63**, 3421–3436.
- Kingsmill, D. E., 1995: Convection initiation associated with a sea-breeze front, a gust front, and their collision. *Mon. Wea. Rev.*, **123**, 2913–2933.
- Kuang, Z., and C. S. Bretherton, 2006: A mass-flux scheme view of a high-resolution simulation of a transition from shallow to deep cumulus convection. *J. Atmos. Sci.*, **63**, 1895–1909.
- Kuo, H. L., 1965: On formation and intensification of tropical cyclones through latent heat release by cumulus convection. *J. Atmos. Sci.*, **22**, 40–63.
- , 1974: Further studies of the parameterization of the influence of cumulus convection on large-scale flow. *J. Atmos. Sci.*, **31**, 1232–1240.
- Mapes, B. E., 2000: Convective inhibition, subgrid-scale triggering energy, and stratiform instability in a toy tropical wave model. *J. Atmos. Sci.*, **57**, 1515–1535.
- , S. Tulich, J. Lin, and P. Zuidema, 2006: The mesoscale convection life cycle: Building block or prototype for large-scale tropical waves? *Dyn. Atmos. Oceans*, **42**, 3–29.
- Neggers, R. A. J., A. P. Siebesma, and H. J. J. Jonker, 2002: A multiparcel model for shallow cumulus convection. *J. Atmos. Sci.*, **59**, 1655–1668.

- Nesbitt, S., and E. J. Zipser, 2003: The diurnal cycle of rainfall and convective intensity according to three years of TRMM measurements. *J. Climate*, **16**, 1456–1475.
- Paluch, I. R., 1979: The entrainment of air in Colorado cumuli. *J. Atmos. Sci.*, **36**, 2467–2478.
- Randall, D. A., Harshvardhan, and D. A. Dazlich, 1991: Diurnal variability of the hydrologic cycle in a general circulation model. *J. Atmos. Sci.*, **48**, 40–62.
- Rio, C., F. Hourdin, J.-Y. Grandpeix, and J.-P. Lafore, 2009: Shifting the diurnal cycle of parameterized deep convection over land. *Geophys. Res. Lett.*, **36**, L07809, doi:10.1029/2008GL036779.
- Sherwood, S. C., and R. Wahrlich, 1999: Observed evolution of tropical deep convective events and their environment. *Mon. Wea. Rev.*, **127**, 1777–1795.
- Sobel, A., 2003: On the coexistence of an evaporation minimum and precipitation maximum in the warm pool. *J. Climate*, **16**, 1003–1009.
- Soden, B. J., 2000: The diurnal cycle of convection, clouds and water vapor in the tropical upper troposphere. *Geophys. Res. Lett.*, **27**, 2173–2176.
- Stensrud, D. J., 1996: Importance of low-level jets to climate: A review. *J. Climate*, **9**, 1698–1711.
- Strokes, G. M., and S. E. Schwartz, 1994: The Atmospheric Radiation Measurement (ARM) program: Programmatic background and design of the cloud and radiation test bed. *Bull. Amer. Meteor. Soc.*, **75**, 1201–1221.
- Tian, B., B. J. Soden, and X. Wu, 2004: Diurnal cycle of convection, clouds, and water vapor in the tropical upper troposphere: Satellites versus a general circulation model. *J. Geophys. Res.*, **109**, D10101, doi:10.1029/2003JD004117.
- Tiedtke, M., 1989: A comprehensive mass flux scheme for cumulus parameterization in large-scale models. *Mon. Wea. Rev.*, **117**, 1779–1800.
- Tompkins, A. M., 2001: Organization of tropical convection in low vertical wind shears: The role of cold pools. *J. Atmos. Sci.*, **58**, 1650–1672.
- Turner, D. D., T. R. Shippert, P. D. Brown, S. A. Clough, R. O. Knuteson, H. E. Revercomb, and W. L. Smith, 1998: Long-term analyses of observed and line-by-line calculations of longwave surface spectral radiance and the effect of scaling the water vapor profile. *Proc. Eighth Atmospheric Radiation Measurement (ARM) Science Team Meeting*, Tucson, AZ, U.S. Department of Energy, 773–776.
- , S. A. Clough, J. C. Liljegren, E. E. Clothiaux, K. E. Cady-Pereira, and K. L. Gaustad, 2007: Retrieving liquid water path and precipitable water vapor from Atmospheric Radiation Measurement (ARM) microwave radiometers. *IEEE Trans. Geosci. Remote Sens.*, **45**, 3680–3690, doi:10.1109/TGRS.2007.903703.
- Wakimoto, R. M., 1982: The life cycle of thunderstorm gust fronts as viewed with Doppler radar and rawinsonde data. *Mon. Wea. Rev.*, **110**, 1060–1082.
- Wesely, M., D. Cook, and R. Coulter, 1995: Surface heat flux data from energy balance Bowen ratio systems. Preprints, *Ninth Symp. on Meteorological Observations and Instrumentation*, Charlotte, NC, Amer. Meteor. Soc., 486–489.
- Wu, C., B. Stevens, and A. Arakawa, 2009: What controls the transition from shallow to deep convection? *J. Atmos. Sci.*, **66**, 1793–1806.
- Xie, S., and Coauthors, 2010: ARM climate modeling best estimate data: A new data product for climate studies. *Bull. Amer. Meteor. Soc.*, **91**, 13–20.
- Yang, G.-Y., and J. M. Slingo, 2001: The diurnal cycle in the tropics. *Mon. Wea. Rev.*, **129**, 784–801.
- Zhang, G. J., and N. A. McFarlane, 1995: Sensitivity of climate simulations to the parameterization of cumulus convection in the Canadian Climate Centre general circulation model. *Atmos.–Ocean*, **33**, 407–446.
- Zhang, Y., and Coauthors, 2008: On the diurnal cycle of deep convection, high-level cloud, and upper troposphere water vapor in the Multiscale Modeling Framework. *J. Geophys. Res.*, **113**, D16105, doi:10.1029/2008JD009905.